



# Facile synthesis of $\text{MnO}_2@ \text{NiCo}_2\text{O}_4$ core–shell nanowires as good performance asymmetric supercapacitor

Xiuhua Wang<sup>1</sup> · Yuan Yang<sup>1</sup> · Peng He<sup>1</sup> · Fuqiang Zhang<sup>1</sup> · Jiping Tang<sup>1</sup> · Zeyu Guo<sup>1</sup> · Ronghui Que<sup>1</sup>

Received: 14 August 2019 / Accepted: 26 November 2019 / Published online: 4 December 2019  
© Springer Science+Business Media, LLC, part of Springer Nature 2019

## Abstract

Hierarchical  $\text{MnO}_2@ \text{NiCo}_2\text{O}_4$  core–shell nanostructures are well fabricated via a simple two-step hydrothermal process. The  $\text{MnO}_2@ \text{NiCo}_2\text{O}_4$  core–shell nanostructures materials electrode presents a high capacitance of  $684 \text{ F g}^{-1}$  at  $2 \text{ A g}^{-1}$  current density, 40 times higher than that of the single  $\text{MnO}_2$  nanowires electrode. And 87.4% retain is approached even at a high current density of  $15 \text{ A g}^{-1}$ , showing satisfactory rate capability. Furthermore, the theoretical analysis reveals the surface capacitance contribution is predominant in the capacitive contribution. The asymmetric supercapacitor assembled with  $\text{MnO}_2@ \text{NiCo}_2\text{O}_4$  exhibited a maximum energy density of  $35.6 \text{ Wh kg}^{-1}$  and a maximum power density of  $745.1 \text{ W kg}^{-1}$ . After 7000 charge–discharge cycling at a current density of  $4 \text{ A g}^{-1}$ , it still can maintain 90% of the initial capacitance. These results suggest that  $\text{MnO}_2@ \text{NiCo}_2\text{O}_4$  is the promising candidate of supercapacitors.

## 1 Introduction

Due to the intensification of environmental pollution and the continuous depletion of fuel energy, it has become an urgent problem to develop green energy storage device to meet the needs of social development [1–3]. Supercapacitors have safe operating voltages and excellent electrochemical performance [4, 5]. There are three kinds of supercapacitor electrodes, which are carbon-based materials [6–8], metal oxide materials [9–11] and conductive polymer materials (polyaniline, polypyrrole, etc.) [12, 13]. Different from carbon-based and conductive polymer electrode materials, transition metal oxides have unique physical and chemical properties, as well as the abundant reserves, low cost, good thermal stability and green pollution-free characteristics. Most of the transition metal oxides have been investigated as

electrochemical energy storage owing to the higher capacitance and energy density [14–19], including cobalt trioxide, nickel oxide, manganese oxide and nickel cobalt oxide ( $\text{NiCo}_2\text{O}_4$ ) [20–23], etc.

Among them,  $\text{MnO}_2$  is easy to synthesize by various synthetic means such as hydrothermal method, electrodeposition, chemical vapor deposition and the like [24–26]. Moreover, it has a variety of morphologies, such as nanowires, nanotubes and nanosheets. In terms of performance,  $\text{MnO}_2$  nanomaterials have good electrical conductivity and outstanding cycle stability. For example, Nam et al. synthesized nano-flowered and nano-wired  $\text{MnO}_2$  by ultrasonic processing with a specific capacitance of  $300 \text{ F g}^{-1}$  at a scan rate of  $5 \text{ mV s}^{-1}$  [27]. Yang et al. prepared amorphous  $\text{MnO}_2$  using potassium permanganate and trihydroxyethylamine, and it showed a specific capacitance of  $251 \text{ F g}^{-1}$  at  $2 \text{ mV s}^{-1}$  scanning rate [28]. However, the capacitance of pure  $\text{MnO}_2$  electrode is generally low and it is difficult to achieve breakthroughs in electrochemical performance. In recent years, some researchers have studied the core–shell nanocomposites with  $\text{MnO}_2$  as the core and other transition metal oxides as the shell [29–31], which exhibiting good supercapacitor performance. Among the transition metal oxides,  $\text{NiCo}_2\text{O}_4$  has the high theoretical capacitance, environmental friendliness and low cost [32–34]. Combining with the nanostructured  $\text{NiCo}_2\text{O}_4$  will exhibit excellent electrochemical performance in energy storage equipment. For example, the  $\text{MnO}_2@ \text{NiCo}_2\text{O}_4$  core/shell nanospheres and  $\text{NiCo}_2\text{O}_4/$

**Electronic supplementary material** The online version of this article (<https://doi.org/10.1007/s10854-019-02649-3>) contains supplementary material, which is available to authorized users.

✉ Xiuhua Wang  
xhwang@mail.ahnu.edu.cn

✉ Ronghui Que  
qrhui123@mail.ahnu.edu.cn

<sup>1</sup> Anhui Key Laboratory of Molecule-Based Materials, The Key Laboratory of Functional Molecular Solids, Ministry of Education, College of Chemistry and Materials Science, Anhui Normal University, Wuhu 241000, China

MnO<sub>2</sub> nanosheet arrays have presented good electrochemical performance in supercapacitors [35, 36].

In this paper, the one-dimensional MnO<sub>2</sub>@NiCo<sub>2</sub>O<sub>4</sub> core-shell nanowires were successfully synthesized by a simple two-step hydrothermal method. As a supercapacitor electrode, the specific capacitance was 684 F g<sup>-1</sup> at 2 A g<sup>-1</sup> current density, and 87.4% remain at higher current density of 15 A g<sup>-1</sup>, exhibiting good rate performance. In addition, MnO<sub>2</sub>@NiCo<sub>2</sub>O<sub>4</sub>, porous carbon and KOH solution were, respectively, used as the positive electrode, negative electrode and electrolyte to assemble the asymmetric supercapacitor. The device exhibited a specific capacitance of 114 F g<sup>-1</sup> at a current density of 1 A g<sup>-1</sup>. The capacitance still remains 90% after 7000 cycles at the current density of 4 A g<sup>-1</sup>. The results show that the one-dimensional MnO<sub>2</sub>@NiCo<sub>2</sub>O<sub>4</sub> core-shell nanowires are promising candidate for excellent supercapacitor material.

## 2 Experimental section

### 2.1 Preparation of MnO<sub>2</sub> nanowires

This is a traditional hydrothermal synthesis process. Ten milliliters of KMnO<sub>4</sub> aqueous solution (0.04 mol/L) and 10 ml of NH<sub>4</sub>Cl aqueous solution (0.04 mol/L) were placed in a beaker and magnetically stirred for 30 min. Next, the mixture was poured in 50-ml Teflon-lined autoclave, sealed and kept at 180 °C for 20 h. After the hydrothermal reaction, the product was washed with deionized water and absolute ethanol, vacuum dried at 60 °C for 12 h to obtain the MnO<sub>2</sub> nanowires.

### 2.2 Synthesis of one-dimensional MnO<sub>2</sub>@NiCo<sub>2</sub>O<sub>4</sub> core-shell nanowires

Specifically, 0.2 mmol of Ni(NO<sub>3</sub>)<sub>2</sub>·6H<sub>2</sub>O, 0.4 mmol of Co(NO<sub>3</sub>)<sub>2</sub>·6H<sub>2</sub>O and 4 mmol of C<sub>6</sub>H<sub>12</sub>N<sub>4</sub> were dissolved in 30 mL of an aqueous ethanol solution (ethanol: deionized

water = 1:1) and magnetically stirred for 30 min to form a pink solution. Then, 0.4 mmol of MnO<sub>2</sub> nanowires was put in the above solution and sonicated for 8 min. Then, the mixture was poured into a 50-ml polytetrafluoroethylene stainless steel autoclave, sealed and heated at 90 °C for 12 h. After the completion of the reaction, the product washed for three times with deionized water and absolute ethanol, dried at 60 °C for 12 h to obtain one-dimensional MnO<sub>2</sub>@NiCo<sub>2</sub>O<sub>4</sub> core-shell nanowires.

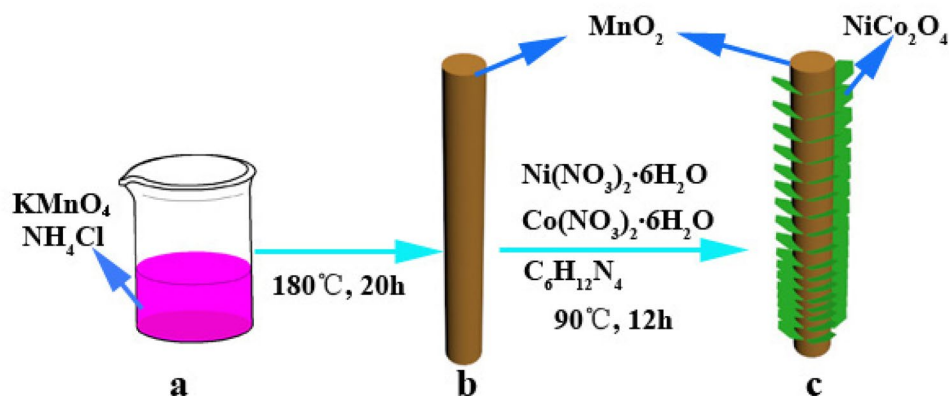
### 2.3 Materials characterization

The morphology of the material was investigated by a scanning electron microscope (FESEM, Hitachi-S4800) at an accelerating voltage of 5 kV. The structure of the material was obtained using a transmission electron microscope (TEM, Hitachi-HT7700) at an accelerating voltage of 100 kV and a high-resolution transmission electron microscope (HRTEM, FEI Tacnai G2) at an acceleration voltage of 200 kV. The crystal structure was obtained by X-ray powder diffraction (XRD) by collecting the patterns using a diffractometer (Bruker D8) equipped with a CuKα radiation source ( $\lambda = 1.54060 \text{ \AA}$ ).

### 2.4 Electrochemical measurements

Electrochemical studies were performed via a CHI 660E electrochemical workstation in 3 M aqueous KOH solution. The process was performed in the three-electrode cell system: the counter electrode of platinum wire, the reference electrode of saturated calomel electrode and the working electrode fabricated by mixing the active material (sample, weight 80%), conductive material (acetylene black, weight 10%) and binder (polytetrafluoroethylene, 10% by weight). The mass loading of the active material was calculated to be about 2.96 mg cm<sup>-2</sup>.

**Scheme 1** Diagram of the synthesis procedure of 1D MnO<sub>2</sub>@NiCo<sub>2</sub>O<sub>4</sub> core-shell nanowire



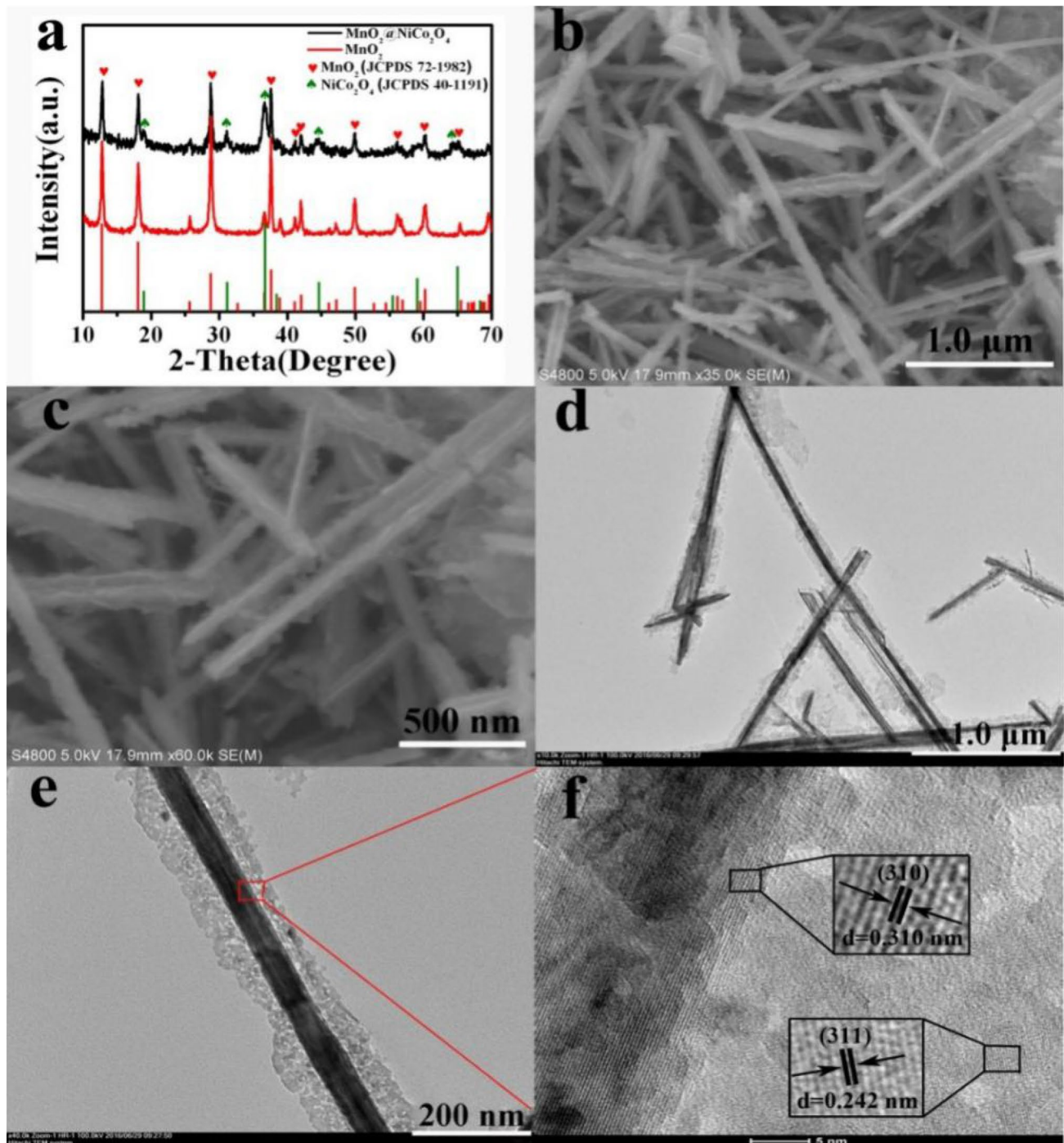


**Fig. 1** a XRD patterns of  $\text{MnO}_2$  and  $\text{MnO}_2@ \text{NiCo}_2\text{O}_4$  core-shell nanowires; b low-magnification SEM image of  $\text{MnO}_2@ \text{NiCo}_2\text{O}_4$ ; c high-magnification SEM morphology of  $\text{MnO}_2@ \text{NiCo}_2\text{O}_4$ ; d the low-

magnification TEM image of  $\text{MnO}_2@ \text{NiCo}_2\text{O}_4$ ; e the high-magnification TEM image of  $\text{MnO}_2@ \text{NiCo}_2\text{O}_4$ ; and f the HRTEM image of  $\text{MnO}_2@ \text{NiCo}_2\text{O}_4$

### 3 Results and discussion

In Scheme 1, the fabrication of hierarchical  $\text{MnO}_2@ \text{NiCo}_2\text{O}_4$  core-shell nanostructures was schematically depicted, involving a simple two-step hydrothermal

synthesis process. Firstly, 10 ml of  $\text{KMnO}_4$  and 10 ml of  $\text{NH}_4\text{Cl}$  were hydrothermally reacted to form brown  $\text{MnO}_2$  nanowires monomers directly (as shown in Scheme 1b). Subsequently, through the second hydrothermal process,  $\text{NiCo}_2\text{O}_4$  nanosheets were grown on the  $\text{MnO}_2$  nanowires

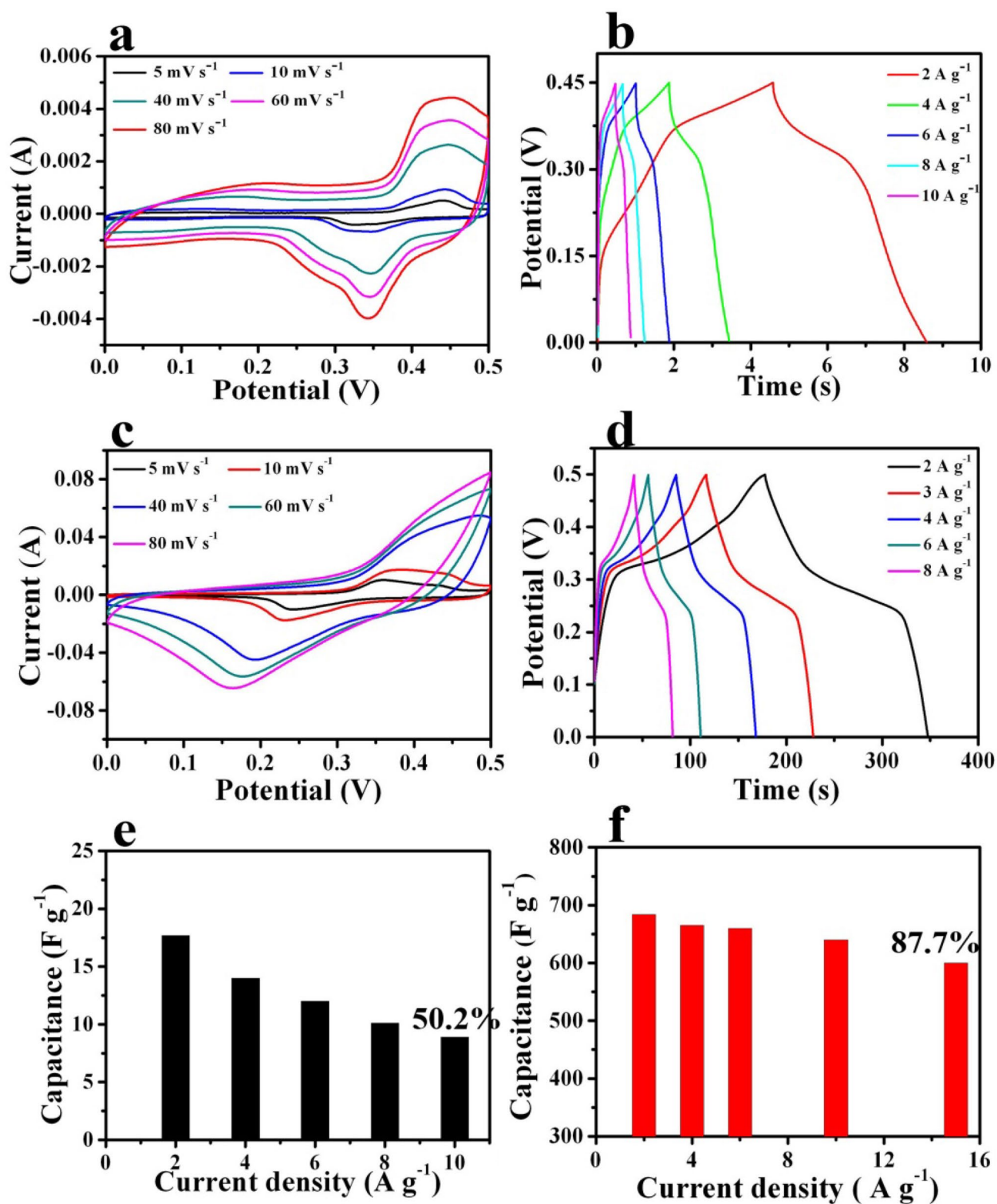


**Fig. 2** **a** CV curves of the MnO<sub>2</sub> electrode at various scan rates; **b** galvanostatic charging and discharging curves of the MnO<sub>2</sub> electrode at a series of current densities; **c** CV curves of the MnO<sub>2</sub>@NiCo<sub>2</sub>O<sub>4</sub> electrode at various scan rates; **d** galvanostatic charge–discharge

curves of the MnO<sub>2</sub>@NiCo<sub>2</sub>O<sub>4</sub> electrode at a series of current densities; the specific capacitance as a function of the current densities of **e** MnO<sub>2</sub> electrode and **f** MnO<sub>2</sub>@NiCo<sub>2</sub>O<sub>4</sub> electrode

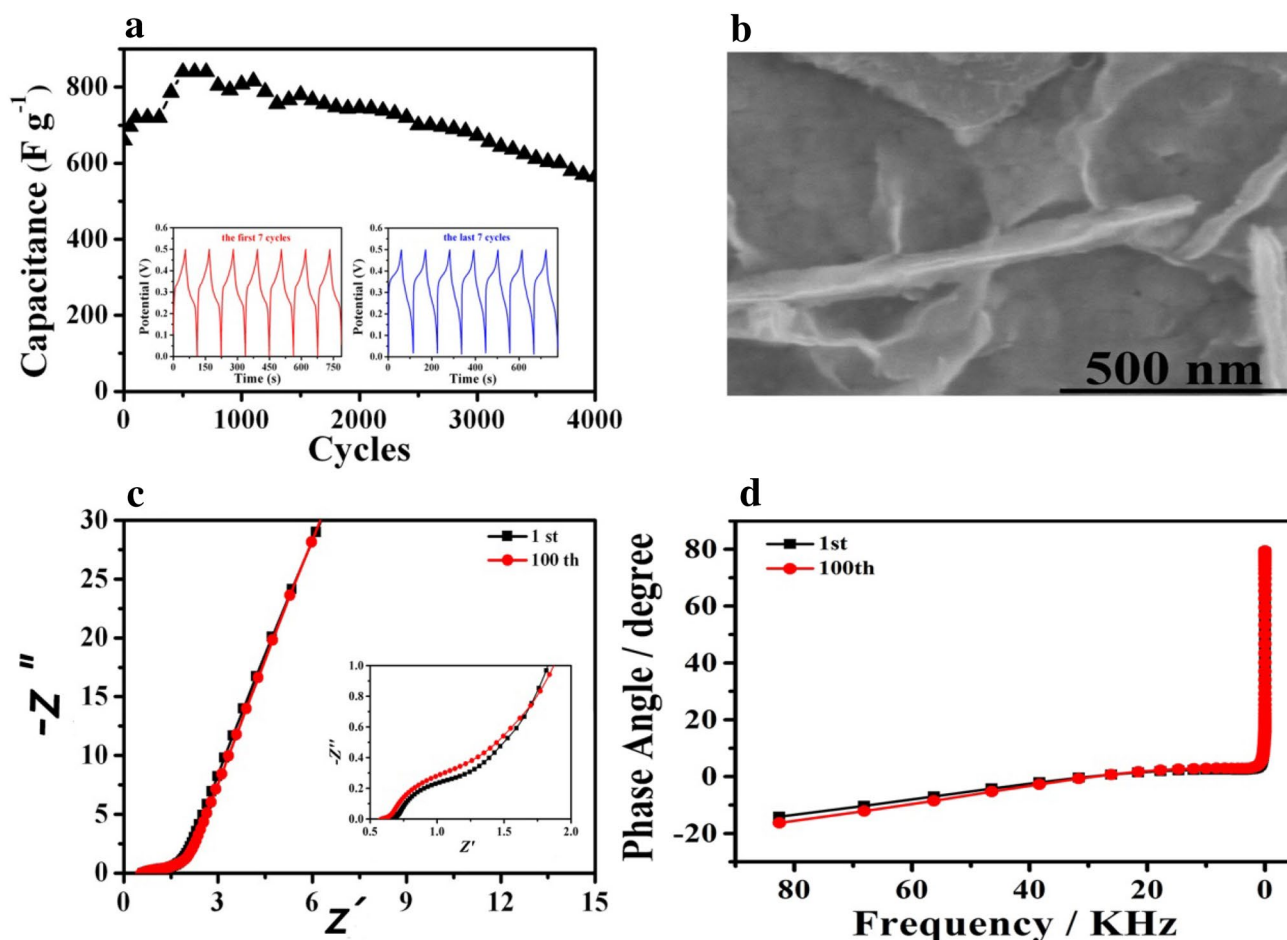


**Fig. 3** **a** Cycling stability of  $\text{MnO}_2@ \text{NiCo}_2\text{O}_4$  electrode at a current density of  $6 \text{ A g}^{-1}$ , insets: the first and last 7 cycling GCD curves; **b** the SEM image of  $\text{MnO}_2@ \text{NiCo}_2\text{O}_4$  electrode after 4000 cycling; **c**

EIS of the electrode at the 1st and 100th cycling, insets: the high frequency; **d** the phase angles for impedance curves of the 1st and 100th cycling

to construct hierarchical one-dimensional  $\text{MnO}_2@ \text{NiCo}_2\text{O}_4$  core-shell nanowires (as shown in Scheme 1c).

Figure 1a shows the diffraction peaks of the  $\text{MnO}_2$  nanowires and  $\text{MnO}_2@ \text{NiCo}_2\text{O}_4$  core-shell nanowires. The peaks located at  $2\theta = 12.7, 18.1, 28.7, 37.6$  and  $50^\circ$  are indexed to the (110), (200), (310), (121) and (411) planes of  $\text{MnO}_2$  (JCPDS File No. 72-1982), respectively. At the same time, the peaks at  $18.9, 31.0, 36.6$  and  $44.5^\circ$  correspond to the (111), (220), (311) and (400) planes of  $\text{NiCo}_2\text{O}_4$ . The results reveal that the chemical compositions of the product are  $\text{MnO}_2$  and  $\text{NiCo}_2\text{O}_4$ .

The SEM and TEM have been performed to study the microstructure of the products. Figure 1b displays the low-magnification SEM image of  $\text{MnO}_2@ \text{NiCo}_2\text{O}_4$ , showing that the  $\text{MnO}_2@ \text{NiCo}_2\text{O}_4$  nanomaterial consists of one-dimensional nanowires with uniform distribution with the average diameter of 130 nm. And the nanosheets are evenly anchored on the surface of the nanowires via the high-magnification

SEM image (Fig. 1c). It is also clearly seen that the nanowires are uniformly covered by the nanosheets to form a layered core-shell nanostructure through the low-magnification TEM morphology (Fig. 1d). And it can be observed that the nanoflakes are composed of very small crystal grains in the high-magnification TEM morphology (Fig. 1e). Figure 1f shows the high-resolution TEM (HRTEM) image of  $\text{MnO}_2@ \text{NiCo}_2\text{O}_4$ . The clear interplanar spacings of 0.310 nm and 0.242 nm are consistent with the (310) plane of  $\text{MnO}_2$  and the (311) plane of  $\text{NiCo}_2\text{O}_4$ , respectively. Based on the above results, we believe that the layered one-dimensional  $\text{MnO}_2@ \text{NiCo}_2\text{O}_4$  nanowires have been successfully synthesized.

The cyclic voltammetry (CV) curves of the  $\text{MnO}_2$  electrode are measured at various scan rates ranging from  $5 \text{ mV s}^{-1}$  to  $80 \text{ mV s}^{-1}$ , as shown in Fig. 2a. There is a distinct redox peak in the CV curve, and no obvious distortion at the high scanning rate of  $80 \text{ mV s}^{-1}$ , exhibiting clearly the pseudocapacitor capacitance property. The GCD

**Table 1** Electrochemical performances comparing between MnO<sub>2</sub>@NiCo<sub>2</sub>O<sub>4</sub> and those literatures reported

Nanomaterials	Capacitance	Capacitance retention	References
MnO <sub>2</sub> /CFP	713.7 F g <sup>-1</sup>	47% from 0.5 to 5 A g <sup>-1</sup>	43
G@MnO <sub>2</sub>	245 F g <sup>-1</sup>	75% from 0.5 to 20 A g <sup>-1</sup>	44
MnO <sub>2</sub> @C	1.49 F cm <sup>-2</sup>	44% from 2 to 16 mA cm <sup>-2</sup>	45
MnO <sub>2</sub> /CNF	445.7 F g <sup>-1</sup>	50.5% from 0.5 to 10 A g <sup>-1</sup>	46
Beta-MnO <sub>2</sub>	362 F g <sup>-1</sup>	87% from 1 to 20 A g <sup>-1</sup>	47
MnO <sub>2</sub> @NiMoO <sub>4</sub>	582 F g <sup>-1</sup>	69% from 1 to 5 A g <sup>-1</sup>	31
MnO <sub>2</sub> @NiCo <sub>2</sub> O <sub>4</sub>	684 F g <sup>-1</sup>	87% from 2 to 15 A g <sup>-1</sup>	Our work

curves of the MnO<sub>2</sub> electrode ranging from 2 to 10 A g<sup>-1</sup> are investigated, as shown in Fig. 2b. The specific capacitance ( $C_m$  (F g<sup>-1</sup>)) of the electrode based on the mass of the active materials is calculated according to the following equations:

$$C_m = \frac{I \times \Delta t}{m \times \Delta V} \quad (1)$$

where  $I$ ,  $\Delta t$ ,  $\Delta V$  and  $m$  are the current (A) during the discharge process, discharge time(s), potential window (V) and mass of the active materials (g), respectively. After calculation, the specific capacitance of the one-dimensional MnO<sub>2</sub> nanowires at current densities of 2, 4, 6, 8 and 10 A g<sup>-1</sup> are 17.7, 14, 12, 10.1 and 8.89 F g<sup>-1</sup>, respectively, as shown in Fig. 2e. Figure S1 shows the comparative CV curves of MnO<sub>2</sub>@NiCo<sub>2</sub>O<sub>4</sub>, acetylene black and nickel foam at a scan rate of 0.8 mV s<sup>-1</sup> in the potential range from 0 to 0.5 V. Obviously, the area of the CV curve enclosed by

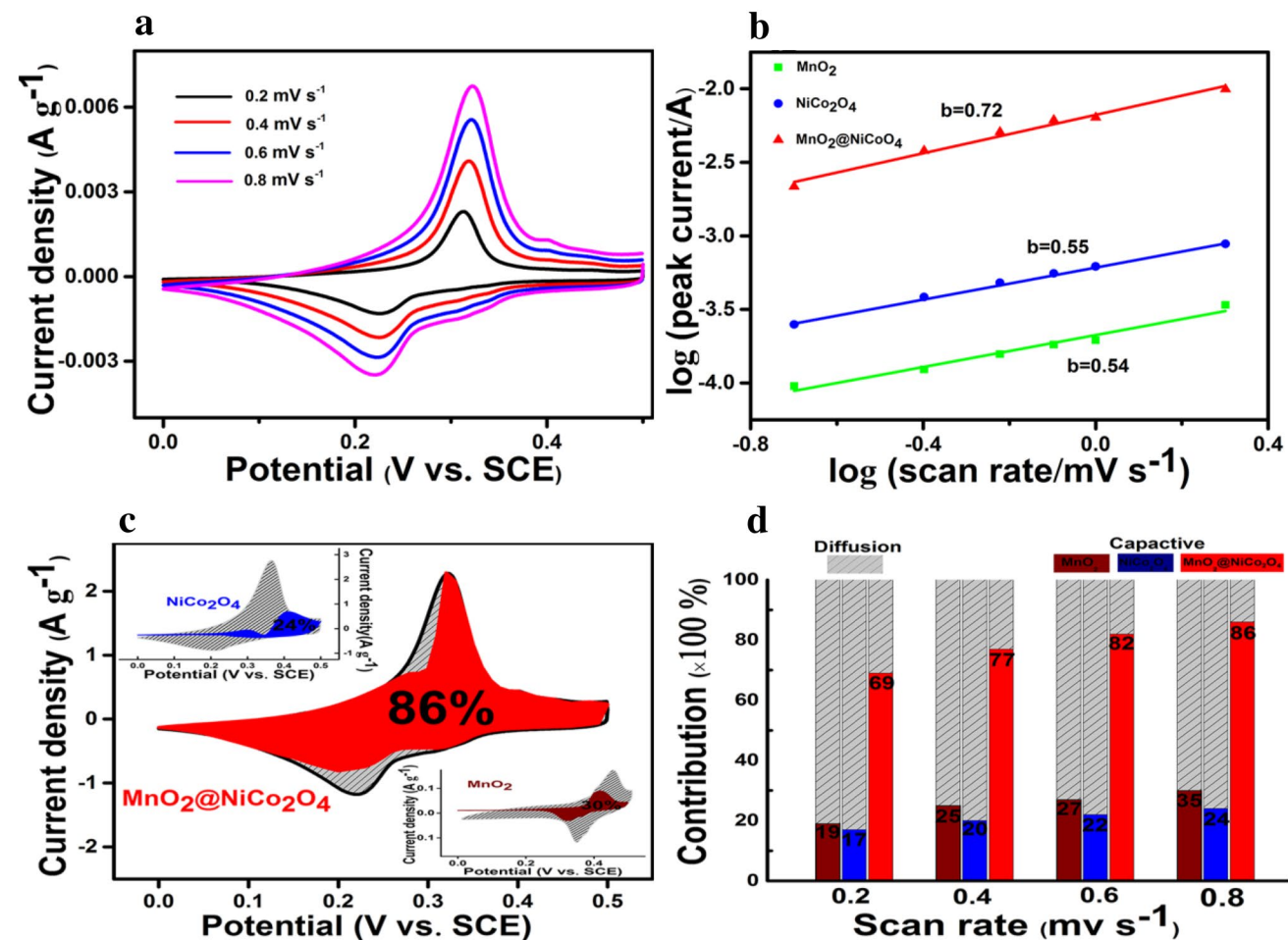


**Fig. 4** a CV curves at different scan rates of the MnO<sub>2</sub>@NiCo<sub>2</sub>O<sub>4</sub> electrode; b relationship between logarithm peak current versus logarithm scan rates; c capacitive contribution (wine for MnO<sub>2</sub>, blue for

NiCo<sub>2</sub>O<sub>4</sub> and red for MnO<sub>2</sub>@NiCo<sub>2</sub>O<sub>4</sub>) and diffusion contribution (gray) at 0.8 mV s<sup>-1</sup>; d the percentage of capacitance contribution at different scan rates

acetylene black or nickel foam is much smaller than that of the  $\text{MnO}_2@/\text{NiCo}_2\text{O}_4$  electrode, indicating that the proportion of capacitance contributed from acetylene black and nickel foam in  $\text{MnO}_2@/\text{NiCo}_2\text{O}_4$  system can be neglected. It is easy to see that the specific capacitance of the  $\text{MnO}_2$  nanowires is low and has small rate capability of 50.2%.

Compared with one-dimensional  $\text{MnO}_2$  nanowires,  $\text{MnO}_2@/\text{NiCo}_2\text{O}_4$  has a significant performance improvement (Fig. 2c). With increasing the scan rate, the peaks of the anode and cathode move toward more negative and positive potentials, respectively, suggesting a quasi-reversible characteristic of the redox reaction. Even at the scan rate of  $80 \text{ mV s}^{-1}$ , the CV curve has no obvious distortion, indicating the ideal CV stability of the  $\text{MnO}_2@/\text{NiCo}_2\text{O}_4$ . Figure 2d shows the GCD performance of the  $\text{MnO}_2@/$

$\text{NiCo}_2\text{O}_4$  electrode at various current densities from 2 to  $8 \text{ A g}^{-1}$ . Clearly, the curves under low current density appear a platform, which represents the redox reactions [37]. The calculated specific capacitances are 684, 665, 660, 640 and  $600 \text{ F g}^{-1}$  at the current densities of 2, 4, 6, 10 and  $15 \text{ A g}^{-1}$ , respectively. It is worth noting that the  $\text{MnO}_2@/\text{NiCo}_2\text{O}_4$  electrode also shows a high specific capacitance of  $600 \text{ F g}^{-1}$  when the current density is up to  $15 \text{ A g}^{-1}$ , exhibiting the excellent rate capacity. In addition, compared to a single  $\text{MnO}_2$ , the specific capacitance of the core-shell electrode at  $2 \text{ A g}^{-1}$  is almost 40 times higher. From the above analysis, it can be stated that the core-shell structure can greatly enhance the electrochemical properties of the material.

For electrode materials, cycling stability is also a very important parameter [38]. After 4000 cycles at a current

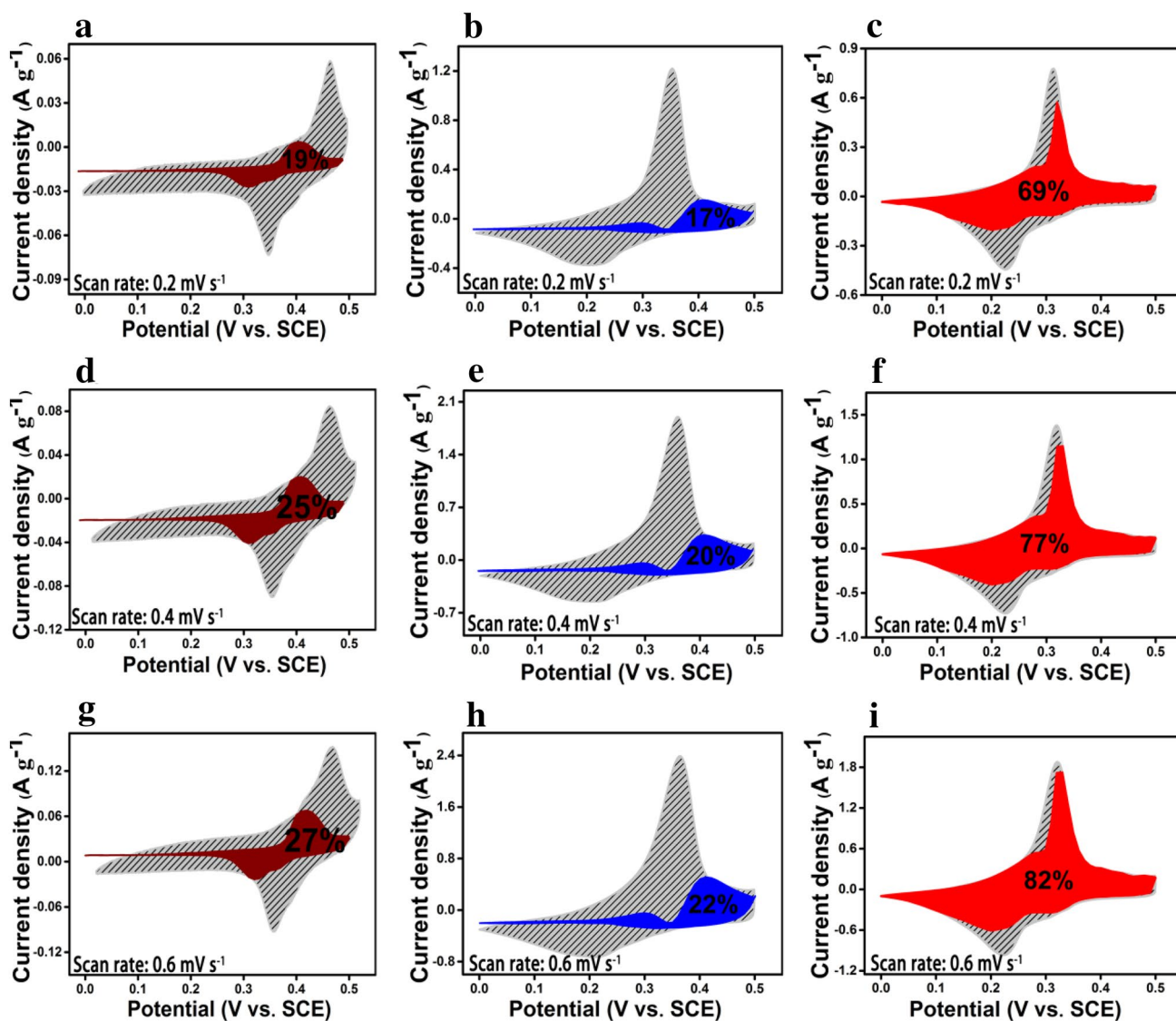


**Fig. 5** Capacitance contribution to charge storage (wine for  $\text{MnO}_2$ , blue for  $\text{NiCo}_2\text{O}_4$  and red for  $\text{MnO}_2@/\text{NiCo}_2\text{O}_4$ ) and diffusion contribution (gray) of different electrode at different scan rates: **a** 0.2, **d** 0.4

and **g**  $0.6 \text{ mV s}^{-1}$  of the  $\text{MnO}_2$ ; **b** 0.2, **e** 0.4 and **h**  $0.6 \text{ mV s}^{-1}$  of the  $\text{NiCo}_2\text{O}_4$ ; **c** 0.2, **f** 0.4 and **i**  $0.6 \text{ mV s}^{-1}$  of the  $\text{MnO}_2@/\text{NiCo}_2\text{O}_4$

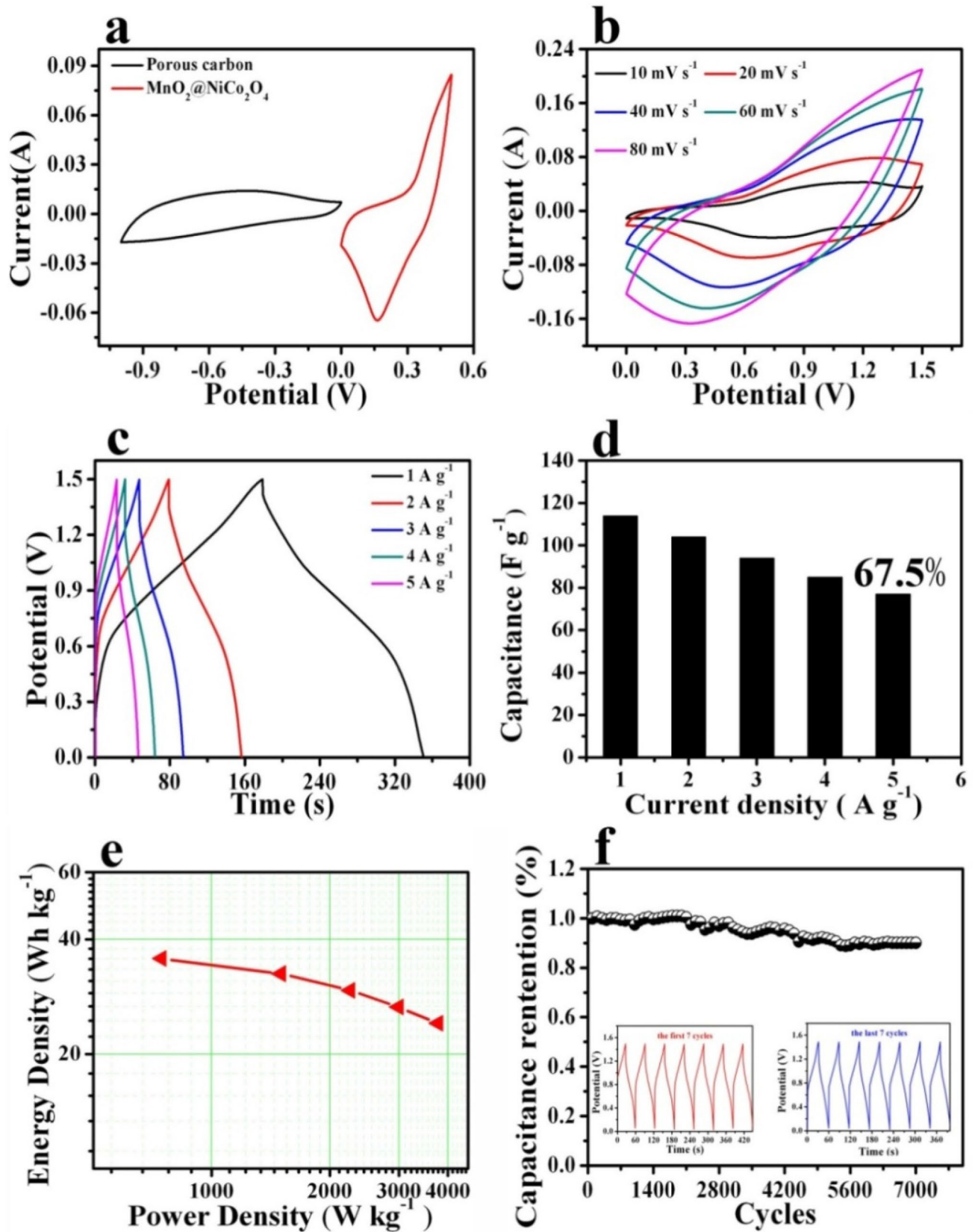




**Fig. 6** **a** CV curves of  $\text{MnO}_2@/\text{NiCo}_2\text{O}_4$  and porous carbon at a scan rate of  $60 \text{ mV s}^{-1}$ ; **b** CV curves of the  $\text{MnO}_2@/\text{NiCo}_2\text{O}_4//\text{C}$  ASC at various scan rates; **c** GCD curves of the  $\text{MnO}_2@/\text{NiCo}_2\text{O}_4//\text{C}$  device at various current densities; **d** the rate performance of the ASC; **e** Ragone plots of the  $\text{MnO}_2@/\text{NiCo}_2\text{O}_4$  device; **f** cycling performances of the  $\text{MnO}_2@/\text{NiCo}_2\text{O}_4//\text{C}$  device, inset: the 1st and last 7 GCD cycles

density of  $6 \text{ A g}^{-1}$ , the  $\text{MnO}_2@/\text{NiCo}_2\text{O}_4$  electrode is capable of retaining 85.6% of the initial specific capacitance, indicating that electrode material has good electrochemical stability, as shown in Fig. 3a. In the first 800 cycles, the capacitance of the electrode material gradually increases to  $850 \text{ F g}^{-1}$ , and the reason could be the activation of the electrode material. Then the capacitance begins to drop slowly. However, after 4000 cycles, it still can retain a capacitance of 85.6%. In order to verify whether the  $\text{MnO}_2@/\text{NiCo}_2\text{O}_4$  electrode morphology transforms after 4000 cycles, the SEM test after cycling was further investigated, as shown in Fig. 3b. By comparison, after 4000 cycles, the core-shell structure still exists and the surface of the  $\text{MnO}_2@/\text{NiCo}_2\text{O}_4$  electrode is considerably rougher. The layered core-shell nanostructures keep stability except for a small amount of collapse during the repeated charging/discharging process, implying that the unique nanostructures can effectively alleviate the volume expansion. First, the 1 dimensional  $\text{MnO}_2$  nanowire core provide a steady structural support during charge-discharge. Second, the interconnected  $\text{NiCo}_2\text{O}_4$  nanosheets provide more void space, which buffering the volume change during charge/discharge [39–41].

Electrochemical impedance spectra (EIS) of the  $\text{MnO}_2@/\text{NiCo}_2\text{O}_4$  electrode before and after 100 cycles were investigated, as shown in Fig. 3c. All Nyquist diagrams consist of two parts, a depressed semicircle in the high-frequency region representing the charge transfer resistance, a slope line in the low-frequency region representing the Warburg impedance attributed to the diffusion resistance of the electrolyte [42]. In the low-frequency region, the  $\text{MnO}_2@/\text{NiCo}_2\text{O}_4$  core-shell nanowire exhibits low Warburg impedance, indicating the facilitated electrolyte diffusion to the surface of the electrodes. The real axis intercept in the high-frequency region represents the volume resistance of the electrochemical system. There was only a slight difference between the 1st and 100th cycling, suggesting the good ion diffusion and conduction kinetics.

Furthermore, the Bode plot of the 1st and 100th cycling also shown in Fig. 3d. It can be found that the operating frequencies of the 1st and 100th cycling are 0.60 and 0.53 Hz, and the corresponding characteristic relaxation time constants ( $\tau_0$ ) are 1.67 and 1.88 s, respectively. The difference between before and after the cycle is small, revealing that the electrode has stable electrolyte permeation and ion diffusion kinetics. Further, it can be seen that

this material has better electrochemical properties than the other  $\text{MnO}_2$ -based electrode materials [31, 43–47], as given in Table 1.

In order to further understand the superior electrochemical performance of the  $\text{MnO}_2@/\text{NiCo}_2\text{O}_4$  core-shell nanowires, we performed a kinetic analysis of the electrochemical. Figure 4a displays the CVs of the  $\text{MnO}_2@/\text{NiCo}_2\text{O}_4$  electrode from 0.2 to  $0.8 \text{ mV s}^{-1}$ . It is known that charge-storage involves two types of mechanisms: the non-faradaic process from the electric double-layer (EDLCs) and the faradaic contribution produced by a redox reaction. The latter can be divided into the diffusion-controlled process and the surface pseudocapacitive contribution arising from the charge transfer at or the near surface [48].

The current ( $i$ ) and scan rate ( $\nu$ ) obey following equation [49]:  $i = a\nu^b$ , where  $a$  is constants, and the value of  $b$  is between 0.5 ~ 1. For a diffusion-controlled process, the  $b$  value is close to 0.5, while for surface pseudocapacitive contribution, the value of  $b$  approach 1. In Fig. 4b, the slope of  $\log i$  versus  $\log \nu$  represents the  $b$  value. The  $b$  value (0.72) of the  $\text{MnO}_2@/\text{NiCo}_2\text{O}_4$  electrode is higher the  $\text{MnO}_2$  and  $\text{NiCo}_2\text{O}_4$ , suggesting that the surface capacitance control capacitance kinetics of  $\text{MnO}_2@/\text{NiCo}_2\text{O}_4$  electrode dominates.

To quantify the contribution from diffusion-controlled process and surface capacitive effect, we can separate the current response ( $i$ ) at a specific potential ( $V$ ) into a diffusion control reaction and a capacitive effect. According to the equation [50, 51]:

$$i(V) = k_1\nu + k_2\nu^{1/2} \quad (2)$$

By drawing  $i(\nu)/\nu^{1/2}$  versus  $\nu^{1/2}$  at multiple potentials, we can get the values of  $k_1$  (slope) and  $k_2$  (intercept) from the straight line to distinguish the ratio of capacitance contribution under different charge-storage mechanisms. The plot of  $i(\nu)/\nu^{1/2}$  versus  $\nu^{1/2}$  has been presented, as shown in Fig. S2. In order to demonstrate the capacitive contribution, the data are obtained at small sweep speeds from 0.2 to  $0.8 \text{ mV s}^{-1}$ . From Fig. 4c, there is a significant fraction of surface capacitive (86%) in the  $\text{MnO}_2@/\text{NiCo}_2\text{O}_4$  core-shell nanowires electrode, much higher than 35% of the  $\text{MnO}_2$  sample and 24% of the  $\text{NiCo}_2\text{O}_4$  sample at the  $0.8 \text{ mV s}^{-1}$ . This result is in good agreement with its higher  $b$  value, suggesting the excellent kinetics of the  $\text{MnO}_2@/\text{NiCo}_2\text{O}_4$  core-shell nanowires electrode. The capacitance contribution of the  $\text{MnO}_2@/\text{NiCo}_2\text{O}_4$  electrode is 69%, 77%, 82% at the scan rate of 0.2, 0.4 and  $0.6 \text{ mV s}^{-1}$  (Fig. 5), respectively, indicating the capacitance-dominated capacitance is leading in the total capacitance. As the sweep speed increases, the surface capacitance contribution gradually increases throughout the current response (Fig. 4d), which is consistent with the expected results.

It is well known that diffusion control behavior occurs primarily in bulk materials or in large dimensions. Therefore, these materials generally exhibit slow kinetic characteristics in electrochemical performance [52]. However, when the material is designed in the nanometer dimension, its electrochemical performance can be significantly improved. For example,  $\text{LiCoO}_2$  from bulk to nanoscale exhibits significant surface capacitance control [53]. For the  $\text{MnO}_2@ \text{NiCo}_2\text{O}_4$  core-shell nanowires, as the outer shell, the nano-sized  $\text{NiCo}_2\text{O}_4$  exposes more active sites, which can more fully contact the electrolyte, shorten the ion transmission distance and accelerate the transmission speed, resulting in a high level of capacitive energy storage.

An asymmetric supercapacitor (ASC) using  $\text{MnO}_2@ \text{NiCo}_2\text{O}_4$  as positive electrode, porous carbon as negative electrode in aqueous 3 M KOH was fabricated. The potential windows of  $\text{MnO}_2@ \text{NiCo}_2\text{O}_4$  and porous carbon are from 0 to 0.5 V and  $-1.0$  to 0 V (Fig. 6a), respectively, indicating the assembled supercapacitor can provide an operating potential of 0–1.50 V in 3 M KOH. As expected, the big operating voltage of the ASC device is stable at 1.5 V, as shown in Fig. 6b. Figure 6c shows the GCD curves of the  $\text{MnO}_2@ \text{NiCo}_2\text{O}_4//\text{C}$ , and the specific capacitances are 114, 104, 94, 85 and 77  $\text{F g}^{-1}$  at current densities of 1, 2, 3, 4 and 5  $\text{A g}^{-1}$ , respectively. The rate performance of the  $\text{MnO}_2@ \text{NiCo}_2\text{O}_4//\text{C}$  asymmetric supercapacitor device is shown in Fig. 6d. The  $\text{MnO}_2@ \text{NiCo}_2\text{O}_4//\text{C}$  device can maintain 67.5% of capacitance retention at a high current density of 5  $\text{A g}^{-1}$ , exhibiting the better rate capability.

Energy density and power density are critical indicators for the practical application of supercapacitors. Ragone plots (energy density vs power density) have been shown in Fig. 6e. The power density and energy density of the ASC were calculated using the following equations:

$$E = \frac{C(\Delta V)^2 \times 1000}{2 \times 3600} \quad (3)$$

$$P = \frac{E \times 3600}{\Delta t \times 1000} \quad (4)$$

Where  $E$  is the energy density,  $C$  represents the specific capacitance of the ASC,  $\Delta V$  refers to the operating voltage of the device,  $\Delta t$  is the discharge time, and  $P$  is the power density. The  $\text{MnO}_2@ \text{NiCo}_2\text{O}_4//\text{C}$  asymmetric supercapacitor exhibits a high energy density of 35.6  $\text{Wh kg}^{-1}$  at power density of 745.1  $\text{W kg}^{-1}$ . When the current density is increased to 5  $\text{A g}^{-1}$ , an energy density can still be maintained at 24.1  $\text{Wh kg}^{-1}$ , while the power density can reach 3772.2  $\text{W kg}^{-1}$ . It can also be seen from the figure that the curve is relatively stable and there is no sharp drop. Therefore, the  $\text{MnO}_2@ \text{NiCo}_2\text{O}_4//\text{C}$  asymmetric supercapacitor has a potential application in high energy density storage.

The cycling stability test of the  $\text{MnO}_2@ \text{NiCo}_2\text{O}_4//\text{C}$  asymmetric supercapacitor was conducted at a current density of 4  $\text{A g}^{-1}$ , as shown in Fig. 6f. The asymmetrical supercapacitor has a stable cycling performance without major fluctuations. After 7000 cycles, the specific capacitance of the ASC retains 90% of initial value. In addition, the 1st and last 7 GCD cycles (the inset of Fig. 6f) have few deformation, suggesting the good cycling performance. All these results demonstrate the good performance of the ASC and the practical application in the energy density storage.

## 4 Conclusions

In summary, we successfully designed  $\text{NiCo}_2\text{O}_4$  nanosheets coated on  $\text{MnO}_2$  nanowires to assemble one-dimensional  $\text{MnO}_2@ \text{NiCo}_2\text{O}_4$  core-shell nanowires by simple two-step hydrothermal method. The electrochemical performance of the core-shell heterostructure is much higher than that of  $\text{MnO}_2$  nanowire monomers. In particular, the specific capacitance of the one-dimensional  $\text{MnO}_2@ \text{NiCo}_2\text{O}_4$  electrode is nearly 40 times higher than that of  $\text{MnO}_2$  at 2  $\text{A g}^{-1}$ , attributed to its unique core-shell structure. And the surface capacitance contribution is leading in the capacitive storage via the kinetically analysis. In addition, the asymmetric supercapacitor device exhibits high energy density of 35.6  $\text{Wh Kg}^{-1}$  with a corresponding power density of 745.1  $\text{W Kg}^{-1}$ . Therefore, the  $\text{MnO}_2@ \text{NiCo}_2\text{O}_4$  core-shell nanowires can be used as potential electrode materials.

**Acknowledgements** The financial support from the National Natural Science Foundation of China (Nos. 21301007 and 21301006) and Anhui Normal University Nurturing Project (No. 2016XJJ001) are acknowledged.

## Compliance with Ethical Standards

**Conflict of interest** The authors declare that they have no conflict of interest.

## References

1. L.-F. Chen, Y. Feng, H.-W. Liang, Z.-Y. Wu, S.-H. Yu, Three-dimensional carbon nanofiber architectures for electrochemical energy storage devices. *Adv Energy Mater* **7**, 201700826 (2017)
2. M. Chen, Y. Zhang, L. Xing, Y. Liao, Y. Qiu, S. Yang, W. Li, Morphology-conserved transformations of metal-based precursors to hierarchically porous micro-/nanostructures for electrochemical energy conversion and storage. *Adv. Mater.* **29**, 201607015 (2017)
3. H. Wang, C. Zhu, D. Chao, Q. Yan, H.J. Fan, Nonaqueous hybrid lithium-ion and sodium-ion capacitors. *Adv. Mater.* **29**, 201702093 (2017)
4. Y. Chen, K. Cai, C. Liu, H. Song, X. Yang, High-performance and breathable polypyrrole coated air-laid paper for flexible all-solid-state supercapacitors. *Adv Energy Mater* **7**, 201701247 (2017)

5. W. Liu, M. Ulaganathan, I. Abdelwahab, X. Luo, Z. Chen, S.J.R. Tan, X. Wang, Y. Liu, D. Geng, Y. Bao, J. Chen, K.P. Loh, Two-dimensional polymer synthesized via solid-state polymerization for high-performance supercapacitors. *ACS Nano* **12**, 852–860 (2018)
6. H. Jia, Y. Cai, X. Zheng, J. Lin, H. Liang, J. Qi, J. Cao, J. Feng, W. Fei, Mesostructured carbon nanotube-on-MnO<sub>2</sub> nanosheet composite for high-performance supercapacitors. *ACS Appl. Mater. Interfaces*. **10**, 38963–38969 (2018)
7. Z. Lu, J. Foroughi, C. Wang, H. Long, G.G. Wallace, Superelastic hybrid CNT/graphene fibers for wearable energy storage. *Adv Energy Mater* **8**, 201702047 (2018)
8. M. Zou, W. Zhao, H. Wu, H. Zhang, W. Xu, L. Yang, S. Wu, Y. Wang, Y. Chen, L. Xu, A. Cao, Single carbon fibers with a macroscopic-thickness, 3D highly porous carbon nanotube coating. *Adv. Mater.* **30**, 201704419 (2018)
9. B.Y. Guan, A. Kushima, L. Yu, S. Li, J. Li, X.W. Lou, Coordination polymers derived general synthesis of multishelled mixed metal-oxide particles for hybrid supercapacitors. *Adv. Mater.* **29**, 201605902 (2017)
10. K. Qiu, M. Lu, Y. Luo, X. Du, Engineering hierarchical nanotrees with CuCo<sub>2</sub>O<sub>4</sub> trunks and NiO branches for high-performance supercapacitors. *J Mater Chem A* **5**, 5820–5828 (2017)
11. R.R. Salunkhe, Y.V. Kaneti, Y. Yamauchi, Metal-organic framework-derived nanoporous metal oxides toward supercapacitor applications: progress and prospects. *ACS Nano* **11**, 5293–5308 (2017)
12. K. Zhou, Y. He, Q. Xu, Q.E. Zhang, A.A. Zhou, Z. Lu, L.-K. Yang, Y. Jiang, D. Ge, X.Y. Liu, H. Bai, A Hydrogel of ultrathin pure polyaniline nanofibers: oxidant-templating preparation and supercapacitor application. *ACS Nano* **12**, 5888–5894 (2018)
13. K. Shu, Y. Chao, S. Chou, C. Wang, T. Zheng, S. Gambhir, G.G. Wallace, “Tandem” strategy to fabricate flexible graphene/polypyrrole nanofiber film using the surfactant-exfoliated graphene for supercapacitors. *ACS Appl. Mater. Interfaces*. **10**, 22031–22041 (2018)
14. D. Dastan, A. Banpurkar, Solution processable sol-gel derived titania gate dielectric for organic field effect transistors. *J. Mater. Sci. - Mater. Electron.* **28**, 3851–3859 (2017)
15. D. Dastan, N. Chaure, M. Kartha, Surfactants assisted solvothermal derived titania nanoparticles: synthesis and simulation. *J. Mater. Sci.* **28**, 7784–7796 (2017)
16. D. Dastan, S.L. Panahi, N.B. Chaure, Characterization of titania thin films grown by dip-coating technique. *J. Mater. Sci.* **27**, 12291–12296 (2016)
17. X.-T. Yin, W.-D. Zhou, J. Li, P. Lv, Q. Wang, D. Wang, F.-Y. Wu, D. Dastan, H. Garmestani, Z. Shi, S. Talu, Tin dioxide nanoparticles with high sensitivity and selectivity for gas sensors at sub-ppm level of hydrogen gas detection. *J. Mater. Sci.* **30**, 14687–14694 (2019)
18. X. Zhu, J. Yang, D. Dastan, H. Garmestani, R. Fan, Z. Shi, Fabrication of core-shell structured Ni@BaTiO<sub>3</sub> scaffolds for polymer composites with ultrahigh dielectric constant and low loss. *Compos. A* **125**, 105521 (2019)
19. D. Dastan, P.U. Londhe, N.B. Chaure, Characterization of TiO<sub>2</sub> nanoparticles prepared using different surfactants by sol-gel method. *J. Mater. Sci.* **25**, 3473–3479 (2014)
20. J. Hao, S. Peng, H. Li, S. Dang, T. Qin, Y. Wen, J. Huang, F. Ma, D. Gao, F. Li, G. Cao, A low crystallinity oxygen-vacancy-rich Co<sub>3</sub>O<sub>4</sub> cathode for high-performance flexible asymmetric supercapacitors. *J Mater Chem A* **6**, 16094–16100 (2018)
21. Z. Wang, F. Wei, Y. Sui, J. Qi, Y. He, Q. Meng, A novel core-shell polyhedron Co<sub>3</sub>O<sub>4</sub>/MnCo<sub>2</sub>O<sub>4.5</sub> as electrode materials for supercapacitors. *Ceram. Int.* **45**, 12558–12562 (2019)
22. P. Balasubramanian, M. Annalakshmi, S.-M. Chen, T. Sathesh, T.-K. Peng, T. Balamurugan, Facile solvothermal preparation of Mn<sub>2</sub>CuO<sub>4</sub> microspheres: excellent electrocatalyst for real-time detection of H<sub>2</sub>O<sub>2</sub> released from live cells. *ACS Appl. Mater. Interfaces*. **10**, 43543–43551 (2018)
23. X.L. Guo, M. Kuang, F. Dong, Y.X. Zhang, Monodispersed plum candy-like MnO<sub>2</sub> nanosheets-decorated NiO nanostructures for supercapacitors. *Ceram. Int.* **42**, 7787–7792 (2016)
24. S. Zhu, L. Li, J. Liu, H. Wang, T. Wang, Y. Zhang, L. Zhang, R.S. Ruoff, F. Dong, Structural directed growth of ultrathin parallel birnessite on beta-MnO<sub>2</sub> for high-performance asymmetric supercapacitors. *ACS Nano* **12**, 1033–1042 (2018)
25. X. Meng, L. Lu, C. Sun, Green synthesis of three-dimensional MnO<sub>2</sub>/graphene hydrogel composites as a high-performance electrode material for supercapacitors. *ACS Appl. Mater. Interfaces*. **10**, 16474–16481 (2018)
26. Qi Gao, Jinxing Wang, Bin Ke, Jingfeng Wang, Yanqiong Li, Fe doped δ-MnO<sub>2</sub> anoneedles as advanced supercapacitor electrodes. *Ceram. Int.* **44**, 18770–18775 (2018)
27. H.-S. Nam, J.-K. Yoon, J.M. Ko, J.-D. Kim, Electrochemical capacitors of flower-like and nanowire structured MnO<sub>2</sub> by a sonochemical method. *Mater. Chem. Phys.* **123**, 331–336 (2010)
28. Y.-J. Yang, E.-J. Liu, L.-M. Li, Z.-Z. Huang, H.-J. Shen, X.-X. Xiang, J Nanostructured amorphous MnO<sub>2</sub> prepared by reaction of KMnO<sub>4</sub> with triethanolamine. *J Alloys Compd* **505**, 555–559 (2010)
29. S. Kim, H.J. Jung, J.C. Kim, K.-S. Lee, S.S. Park, V.P. Dravid, K. He, H.Y. Jeong, In situ observation of resistive switching in an asymmetric graphene oxide bilayer structure. *ACS Nano* **12**, 7335–7342 (2018)
30. X. Lu, C. Shen, Z. Zhang, E. Barrios, L. Zhai, Core-shell composite fibers for high-performance flexible supercapacitor electrodes. *ACS Appl. Mater. Interfaces*. **10**, 4041–4049 (2018)
31. X. Wang, H. Xia, J. Gao, B. Shi, Y. Fang, M. Shao, Enhanced cycle performance of ultraflexible asymmetric supercapacitors based on a hierarchical MnO<sub>2</sub>@NiMoO<sub>4</sub> core-shell nanostructure and porous carbon. *J Mater Chem A* **4**, 18181–18187 (2016)
32. D.S. Sun, Y.H. Li, Z.Y. Wang, X.P. Cheng, S. Jaffer, Y.F. Zhang, Understanding the mechanism of hydrogenated NiCo<sub>2</sub>O<sub>4</sub> nanogross supported on Ni foam for enhanced-performance supercapacitors. *J Mater Chem A* **4**, 5198–5204 (2016)
33. S. Sun, S. Wang, S. Li, Y. Li, Y. Zhang, J. Chen, Z. Zhang, S. Fang, P. Wang, Asymmetric supercapacitors based on a NiCo<sub>2</sub>O<sub>4</sub>/three dimensional graphene composite and three dimensional graphene with high energy density. *J Mater Chem A* **4**, 18646–18653 (2016)
34. F.-X. Ma, L. Yu, C.-Y. Xu, X.W. Lou, Self-supported formation of hierarchical NiCo<sub>2</sub>O<sub>4</sub> tetragonal microtubes with enhanced electrochemical properties. *Energy Environ. Sci.* **9**, 862–866 (2016)
35. Y. Zhou, L. Ma, M.Y. Gan, M.H. Ye, X.R. Li, Y.F. Zhai, F.B. Yan, F.F. Cao, Monodisperse MnO<sub>2</sub>@NiCo<sub>2</sub>O<sub>4</sub> core/shell nanospheres with highly opened structures as electrode materials for good-performance supercapacitors. *Appl. Surf. Sci.* **444**, 1–9 (2018)
36. S.W. Zhang, B.S. Yin, C. Liu, Z.B. Wang, D.M. Gu, Self-assembling hierarchical NiCo<sub>2</sub>O<sub>4</sub>/MnO<sub>2</sub> nanosheets and MoO<sub>3</sub>/PPY core-shell heterostructured nanobelts for supercapacitor. *Chem Engin J* **312**, 296–305 (2017)
37. X. Wang, B. Shi, Y. Fang, F. Rong, F. Huang, R. Que, M. Shao, High capacitance and rate capability of a Ni<sub>3</sub>S<sub>2</sub>@CdS core-shell nanostructure supercapacitor. *J Mater Chem A* **5**, 7165–7172 (2017)
38. J. Han, Y. Dou, J. Zhao, M. Wei, D.G. Evans, X. Duan, Flexible CoAl LDH@PEDOT core/shell nanoplatelet array for high-performance energy storage. *Small* **9**, 98–106 (2013)
39. D. Zhao, X. Wu, C. Guo, Hybrid MnO<sub>2</sub>@NiCo<sub>2</sub>O<sub>4</sub> nanosheets for high performance asymmetric supercapacitors. *Inorg Chim Front* **5**, 1378–1385 (2018)

40. Z. Ma, G. Shao, Y. Fan, M. Feng, D. Shen, H. Wang, Fabrication of high-performance all-solid-state asymmetric supercapacitors based on stable  $\alpha$ - $\text{MnO}_2$ @ $\text{NiCo}_2\text{O}_4$  core shell heterostructure and 3D-nanocage N-doped porous carbon. *ACS Sustain Chem Eng* **5**, 4856–4868 (2017)
41. L. Su, L. Hou, S. Di, J. Zhang, X. Qin, Plumage-like  $\text{MnO}_2$ @ $\text{NiCo}_2\text{O}_4$  core-shell architectures for high-efficiency energy storage: the synergistic effect of ultralong  $\text{MnO}_2$  “scaffold” and ultrathin  $\text{NiCo}_2\text{O}_4$  “fluff”. *Ionics* **24**, 3227–3235 (2018)
42. L. Peng, X. Ji, H. Wan, Y. Ruan, K. Xu, C. Chen, L. Miao, J. Jiang, Nickel sulfide nanoparticles synthesized by microwave-assisted method as promising supercapacitor electrodes: an experimental and computational study. *Electrochim. Acta* **182**, 361–367 (2015)
43. W. Dang, C. Dong, Z. Zhang, G. Chen, Y. Wang, H. Guan, Self-grown  $\text{MnO}_2$  nanosheets on carbon fiber paper as high-performance supercapacitors electrodes. *Electrochim. Acta* **217**, 16–23 (2016)
44. L. Wang, Y. Ouyang, X. Jiao, X. Xia, W. Lei, Q. Hao, Polyaniline-assisted growth of  $\text{MnO}_2$  ultrathin nanosheets on graphene and porous graphene for asymmetric supercapacitor with enhanced energy density. *Chem Engin J* **334**, 1–9 (2018)
45. D. Wu, S. Xu, M. Li, C. Zhang, Y. Zhu, Y. Xu, W. Zhang, R. Huang, R. Qi, L. Wang, P.K. Chu, Hybrid  $\text{MnO}_2/\text{C}$  nano-composites on a macroporous electrically conductive network for supercapacitor electrodes. *J Mater Chem A* **3**, 16695–16707 (2015)
46. N. Zhang, C. Fu, D. Liu, Y. Li, H. Zhou, Y. Kuang, Three-dimensional pompon-like  $\text{MnO}_2$ /graphene hydrogel composite for supercapacitor. *Electrochim. Acta* **210**, 804–811 (2016)
47. S. Zhu, H. Zhang, P. Chen, L.-H. Nie, C.-H. Li, S.-K. Li, Self-assembled three-dimensional hierarchical graphene hybrid hydrogels with ultrathin  $\beta$ - $\text{MnO}_2$  nanobelts for high performance supercapacitors. *J Mater Chem A* **3**, 1540–1548 (2015)
48. X. Xia, D. Chao, Y. Zhang, J. Zhan, Y. Zhong, X. Wang, Y. Wang, Z.X. Shen, J. Tu, H.J. Fan, Generic synthesis of carbon nanotube branches on metal oxide arrays exhibiting stable high-rate and long-cycle sodium-ion storage. *Small* **12**, 3048–3058 (2016)
49. H. Lindstrom, S. Sodergren, A. Solbrand, H. Rensmo, J. Hjelm, A. Hagfeldt, S.E. Lindquist, *J Phys Chem B* **101**, 7717–7722 (1997)
50. J. Wang, J. Polleux, J. Lim, B. Dunn, Pseudocapacitive contributions to electrochemical energy storage in  $\text{TiO}_2$  (anatase) nanoparticles. *J. Phys. Chem. C* **111**, 14925–14931 (2007)
51. M. Sathiy, A.S. Prakash, K. Ramesha, J.M. Tarascon, A.K. Shukla,  $\text{V}_2\text{O}_5$ -anchored carbon nanotubes for enhanced electrochemical energy storage. *J. Am. Chem. Soc.* **133**, 16291–16299 (2011)
52. P. Simon, Y. Gogotsi, B. Dunn, Where do batteries end and supercapacitors begin. *Science* **343**, 1210–1211 (2014)
53. V. Augustyn, P. Simon, B. Dunn, Pseudocapacitive oxide materials for high-rate electrochemical energy storage. *Energy Environ. Sci.* **7**, 1597–1614 (2014)

**Publisher's Note** Springer Nature remains neutral with regard to jurisdictional claims in published maps and institutional affiliations.